Defining the Proton Topology of the Zr$_6$-Based Metal−Organic Framework NU-1000

Nora Planas,[†,∥] Joseph E. Mondloch,[‡,∥] Samat Tussupbayev,[†] Joshua Borycz,[†] Laura Gagliardi,*[,†] Joseph T. Hupp,*[,‡] Omar K. Farha,*[,‡,§] and Christopher J. Cramer*[,†]

[†]Department of Chemistry, Supercomputing Institute, and Chemical Theory Center, University of Minnesota, Minneapolis, Minnesota 55455, United States

[‡]Department of Chemistry, Northwestern University, 2145 Sheridan Road, Evanston, Illinois 60208, United States

[§]Department of Chemistry, Faculty of Science, King Abdulaziz University, Jeddah, Saudi Arabia

Ⓢ *Supporting Information*

ABSTRACT: Metal−organic frameworks (MOFs) constructed from Zr$_6$-based nodes have recently received considerable attention given their exceptional thermal, chemical, and mechanical stability. Because of this, the structural diversity of Zr$_6$-based MOFs has expanded considerably and in turn given rise to difficulty in their precise characterization. In particular it has been difficult to assign where protons (needed for charge balance) reside on some Zr$_6$-based nodes. Elucidating the precise proton topologies in Zr$_6$-based MOFs will have wide ranging implications in defining their chemical reactivity, acid/base characteristics, conductivity, and chemical catalysis. Here we have used a combined quantum mechanical and experimental approach to elucidate the precise proton topology of the Zr$_6$-based framework NU-1000. Our data indicate that a mixed node topology, [Zr$_6(\mu_3$−O)$_4(\mu_3$−OH)$_4$(OH)$_4$ (OH$_2)_4$]$^{8+}$, is preferred and simultaneously rule out five alternative node topologies.

SECTION: Surfaces, Interfaces, Porous Materials, and Catalysis
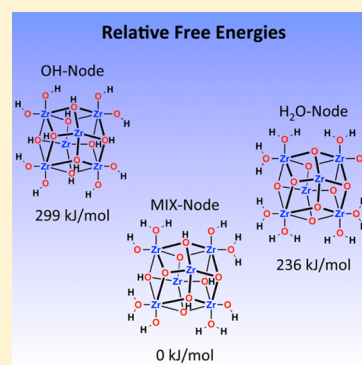
Over the past two decades, considerable attention has been drawn to the powerful attributes of metal−organic frameworks (MOFs) given their structural, as well as chemical, versatility and hence tailorability.[1−3] Because of their crystalline nature, unambiguous structural determination is often possible for MOFs; this in turn has facilitated precise mechanistic studies[4−6] and in the most favorable cases predictive materials discovery.[7,8] Recently, a new class of MOFs containing octahedral Zr$_6$ clusters and multitopic carboxylate linkers (R−(CO$_2^-$)$_n$, n = 2, 3, 4) has emerged.[9−11] Profiting from strong coordination bonds between the hard acid-hard base interactions of the Zr^{IV} atoms and carboxylate oxygens, Zr$_6$-based MOFs exhibit exceptional thermal (up to 500 °C),[9] chemical (e.g., from pH 1−pH 11),[12] and even mechanical stability.[9,13] Given these properties, Zr$_6$-based MOFs have been investigated for several applications including gas sorption,[14,15] catalysis,[16−19] heavy metal capture,[20,21] sensing,[12] ionic conductivity,[22] toxic industrial chemical capture,[23] and water sorption.[11]

An intriguing subclass of Zr$_6$-based MOFs are built up from 2D Kagome sheets of eight-connected [Zr$_6(\mu_3$−O)$_8$(O)$_8$(H)$_{16}$]$^{8+}$ nodes bridged by tetra-carboxylate linkers (R−(CO$_2^-$)$_4$); an example of this topology is shown in Figure 1a−d.[10,24−26] Such a connectivity gives rise to 3D structures with −OH containing (i.e., −OH or −OH$_2$, vide infra) functional groups pointing into exceptionally large 1-D mesoporous channels. As a result, this class of Zr$_6$-based
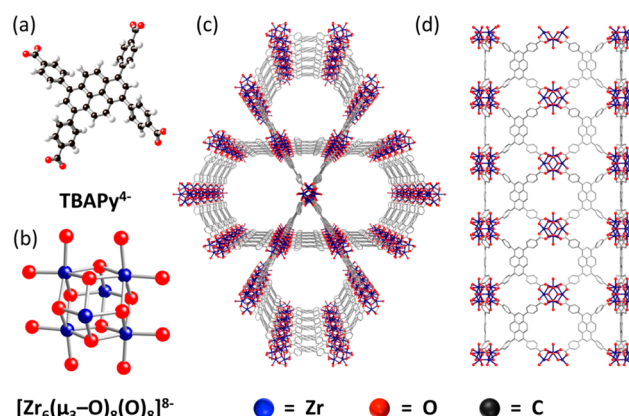

Figure 1. 1,3,6,8-Tetrakis(*p*-benzoic acid)pyrene linker, TBAPy^{4-} (a) and the [Zr$_6(\mu_3$−O)$_8$(O)$_8$]$^{8-}$ node (b) of the Zr$_6$-based framework NU-1000 (c and d). Note that the linkers are not shown in the representation of the node, and the hydrogens are not shown in the framework representations for clarity.

MOFs has been particularly susceptible to a variety of postsynthesis modification schemes. Examples include metal-

ation at the organic linker,[10] metalation at the nodes via Atomic layer deposition In a Metal−organic framework (AIM),[26] and organic functionalization at the node via Solvent-Assisted Ligand Incorporation (SALI).[27,28] To date, these postsynthesis modified materials have facilitated catalysis,[24,26] enhanced CO_2 adsorption,[27] and been susceptible toward secondary organic functionalization.[28]

Despite the intriguing nature of these frameworks, a less well understood aspect is the precise proton topology of these eight-connected Zr_6 nodes. That is, it has been difficult to assign precisely where the 16 protons (needed for charge balance) reside in the $[Zr_6(\mu_3\text{-}O)_8(O)_8]^{8-}$ node. As an example, both Morris et al. (MOF-545) and Feng et al. (PCN-222) synthesized tetra-carboxylate porphyrin containing Zr_6-based frameworks.[10,24] Based on single-crystal X-ray diffraction, Morris et al. assigned the 16 protons as eight terminal H_2O molecules ($[Zr_6(\mu_3\text{-}O)_8(H_2O)_8]^{8+}$), while Feng et al. assigned the protons as bridging and terminal −OH groups ($[Zr_6(\mu_3\text{-}OH)_8(OH)_8]^{8+}$).[29] Given the ambiguities associated with locating protons in single-crystal structural analysis, we recently utilized IR spectroscopy to obtain data consistent with the presence of both terminal and μ_3-bridging −OH groups in tetracarboxylate pyrene-based Zr_6 MOF NU-1000.[26]

Herein we use a combined quantum mechanical and experimental approach to rigorously assign the proton topology of our recently synthesized Zr_6-based framework, NU-1000. We find that the Zr_6-based node of NU-1000 actually comprises a staggered mixed proton topology, namely $[Zr_6(\mu_3\text{-}O)_4(\mu_3\text{-}OH)_4(OH)_4(H_2O)_4]^{8+}$. En route to this mixed proton topology, we ruled out five additional proton topologies. This is the first time a mixed −OH, −OH_2 composition has been observed for a symmetric Zr_6-based node, which we suspect will be of paramount importance for understanding the reactivity (e.g., in AIM and SALI), conductivity, and catalytic activity of these unique materials.

Periodic Systems. Starting from the known experimental single-crystal X-ray structure, the periodic structures for NU-1000-OH, NU-1000-OH_2, and NU-1000-MIX-X (Figure 2 where X = S, L, C, and E) were fully optimized using periodic density functional theory as implemented in the Vienna Ab
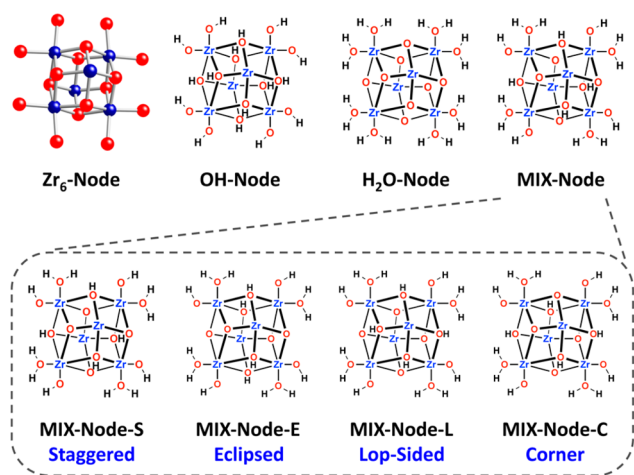
Initio Simulation Package (VASP)[30−33] employing the generalized gradient approximation exchange-correlation functional PBE.[34−36] The VASP calculations use projector-augmented wave potentials to describe the interaction between core and valence electrons. A plane-wave kinetic energy cutoff of 520 eV was used, and the integration over the irreducible Brillouin zone was carried out using the gamma point. The energy convergence cutoff was 1×10^{-6} eV. Atomic positions were relaxed until the forces were lower than 0.05 eV Å^{-1} including accounting for Pulay stress.

Cluster Model. We extracted from the optimized periodic structures of NU-1000-OH, NU-1000-OH_2, and NU-1000-MIX-X (X = S, L, C, and E), corresponding model clusters having the general formula $[Zr_6(\mu_3\text{−}OH)_8(OH)_8(PhCOO)_8]$ (OH-Node), $[Zr_6(\mu_3\text{-}O)_8(OH_2)_8(PhCOO)_8]$ (H$_2$O-Node) and $[Zr_6(\mu_3\text{-}O)_4(\mu_3\text{-}OH)_4(OH)_4(OH_2)_4(PhCOO)_8]$ (MIX-Node-X; X = S, L, C, and E). These clusters were designed to maintain an overall neutral charge for the model system as well as to preserve a good representation of the first coordination sphere of the Zr_6 oxo-metalate node in the periodic structure. We note that the TBAPy^{4-} linkers (1,3,6,8-tetrakis(*p*-benzoate)pyrene) have been replaced with benzoate (PhCOO$^-$) groups having their carbon atoms constrained to corresponding positions of the TBAPy^{4-} framework.

Two-step constrained geometry optimizations were performed for these clusters. In the first step, all of the aromatic H atom positions were optimized (since one is not present in the periodic structure) while all of the other atoms were held fixed. In the second step, the 6 Zr, 16 O, 16 protonating H$^+$ nuclei, and the four carboxylic COO$^-$ functionalities were allowed to relax in the presence of the fixed linker fragments so as to mimic the solid-state framework.

Cluster Calculations. DFT cluster calculations used the M06-L[37] density functional as implemented in the Gaussian 09 software package.[38,39] An ultrafine grid (99 radial nodes and 590 angular nodes) was used to perform numerical integrations. An automatic density-fitting set generated by the Gaussian program was used to reduce the cost for calculations done with the local density functional M06-L. The 6-31G(d,p)[40] basis set was used for H, C, and O, while the Stuttgart [8s7p6d1f | 6s5p3d1f] ECP10MDF contracted effective core potential basis set (SDD)[40,41] was employed for Zr. Single-point calculations were performed with the 6-311+G(df,p)[40] basis set for H, C, and O and the SDD basis set for Zr. The SMD[42] continuum solvent model was employed to account for solvation with water as a solvent. The nature of all stationary points was verified by analytical computation of vibrational frequencies; IR spectra were computed employing a scale factor of 0.939 for fundamentals.

Materials. All compounds and solvents were used as received unless otherwise noted: 1,3,6,8-tetrakis(*p*-benzoic acid)pyrene was synthesized as previously described,[26] acetone (Macron, 98%), benzoic acid (Aldrich, 99.5%), *N,N*-dimethylformamide (DMF) (Macron, 99.8%), hydrochloric acid (Aldrich, 37%), ZrOCl$_2$•8H$_2$O (Aldrich, 98%).

Instrumentation. Diffuse reflectance infrared spectra (DRIFTS) were recorded on a Nicolet 7600 FTIR spectrometer equipped with an MCT detector. The detector was cooled with liquid N$_2$. The spectra were either collected under Ar atmosphere or in a KBr mixture under N$_2$ purge. KBr or NU-1000 (difference spectra) were utilized as background spectra. Powder X-ray diffraction (PXRD) measurements were carried out on a Bruker MX *IμS* microsource with Cu Kα

Figure 2. Top, schematic representation of the three structural isomers (OH-Node, H$_2$O-Node, and MIX-Node) considered herein. Bottom, schematic representation of four conformers considered for the MIX-Node isomer. The aromatic carboxylate linkers have been omitted for clarity.

radiation and an Apex II CCD detector. The samples were mounted in capillaries as powders in a glovebox, sealed with epoxy, brought out of the glovebox and placed on a goniometer head. The data were collected on an area detector with rotation frames over 180° in ϕ and at 2θ values of 12, 24, and 36° being exposed for 10 min at each frame. Overlapping sections of data were matched, and the resulting pattern was integrated using Bruker's APEX2 phase ID program. The powder patterns were treated for amorphous background scatter. Thermal gravimetric analysis (TGA) was performed on a Mettler Toledo TGA under N_2 flow and heated from room temperature to 700 °C (at 10 °C min^{-1}).

Synthesis of NU-1000. NU-1000 was synthesized as a microcrystalline powder using a slightly modified procedure to that previously published.[26] Briefly, 0.097 g of $ZrOCl_2 \cdot 8H_2O$ (0.30 mmol) was weighed out into a 6-dram vial and 2.7 g of benzoic acid was subsequently added. The solids were dissolved via sonication in 8 mL of DMF and placed in an oven at 80 °C for 1 h. After 1 h the solution was taken out of the oven, allowed to cool, and then 0.040 g of H_4TBAPy was added into the vial and sonicated until a homogeneous yellow suspension was obtained. The yellow suspension was placed in an oven at 100 °C for 24 h and then the mother liquor was decanted. The resultant yellow powder was washed with 10 mL of DMF three times over the course of 24 h. Centrifugation (7000 rpms for 5 min in Eppendorf tubes) was utilized to separate the liquid and solid phases in between washings. The solid was resuspended in 12 mL of DMF and 0.5 mL of 8 M HCl was added to the solution and swirled. The vial was placed in the oven at 100 °C for 18 h and then removed. Again the mother liquor was decanted, and the yellow powder was washed three times with 10 mL of DMF over the course of 24 h and then 10 mL of acetone three times over the course of 24 h. Prior to physical measurements the samples were activated under dynamic vacuum at 120 °C until a vacuum level of ≤0.002 mmHg min^{-1} was reached. PXRD, TGA, and N_2 adsorption isotherms corroborated many of the previously reported structural details regarding NU-1000 (Figure 1).[26,43]

Diffuse Reflectance Infrared Fourier Transform Spectroscopy (DRIFTS). For the room temperature measurements approximately 0.5 mg of sample was gently ground and mixed with 20 mg of finely ground KBr. For the temperature-dependent measurements approximately 0.03 g of sample was gently ground and placed in a Harrick praying mantis cell. The cell was cooled in a liquid ice bath. The temperature was increased to the desired temperature, and the spectra were monitored until no further changes were observed. Subsequently, the sample was cooled back down to 25 °C, and the spectra were monitored until no further changes were observed. All reported spectra were collected at 25 °C.

D_2O Exchange Experiments. NU-1000 (0.015 g) was placed in 2 mL of D_2O for 72 h. The solution was decanted and replaced three times over the course of the experiment. Subsequently, the D_2O was exchanged with d_6-acetone (three times over the course of 24 h). Finally the d_6-acetone was removed under dynamic vacuum overnight at 100 °C.

Probing the Proton Topology of NU-1000 via Quantum Chemical Calculations. To ensure neutrality of the $[Zr_6(\mu_3-O)_8(O)_8(RCO_2^-)_8]^{16-}$ node, 16 protons were placed in three distinct oxygen-based environments of NU-1000. The results are schematically summarized in Figure 2 (top) and yield the following structural isomers: (i) the −OH isomer, $[Zr_6(\mu_3-OH)_8(OH)_8]^{8+}$ (periodic; NU-1000-OH and cluster; OH-

node); (ii) the $-OH_2$ isomer $[Zr_6(\mu_3-O)_8(H_2O)_8]^{8+}$ (periodic; NU-1000-OH_2 and cluster; H_2O-Node), and (iii) the −MIX isomer exhibiting the formula $[Zr_6(\mu_3-O)_4(\mu_3-OH)_4(OH)_4(H_2O)_4]^{8+}$ (periodic; NU-1000-MIX and cluster; MIX-Node). In the MIX-node case, there are four additional tautomers which have been labeled by referring to the relative position of the four μ_3-OH ligands which could be staggered (MIX-Node-S), eclipsed (MIX-Node-E), lop-sided (MIX-Node-L) or contiguous in opposite corners (MIX-Node-C) as illustrated in Figure 2.

We performed quantum chemical calculations with both periodic and cluster models under different geometry constraints to compute the relative energies for each isomer. The unit cell parameters for NU-1000-OH, NU-1000-OH_2, and NU-1000-MIX-X (X = S, E, L, and C), as well as the parameters from single crystal X-ray diffraction, are listed in Table S1. As shown in Table 1, the relative energies from the

Table 1. Relative Energies (kJ mol^{-1}) for the Constitutional Isomers and Conformers Studied Herein[a]

NU-1000- or model-node topology	ΔE periodic	ΔE cluster[b,c]	ΔG cluster[b]
−OH	350	334 (214)	299
$-OH_2$	274	274 (218)	236
−MIX-Node-S	0	0 (0)	0
−MIX-L	249	255 (145)	235
−MIX-C	139	154 (105)	150
−MIX-E (30)[d]	122	146 (106)	150
−MIX-E (8)[d]	140	153 (107)	147

[a]Full geometry optimizations were performed by periodic calculations employing PBE and constrained optimizations were performed with cluster models using M06L/SDD(Zr)|6-311+G(df,p)(C,H,O)//M06L/SDD(Zr)|6-31G(d,p)(C,H,O) DFT functional. [b]Restrained Ph ring positions. [c]Values in parentheses include continuum aqueous solvation effects. [d]The E isomers differ with respect to orienting the core protons either into the 30 or 8 Å pores of NU-1000.

constrained cluster optimizations are in good agreement with the energies from the periodic calculations (average deviation over 7 structures is 10 kJ/mol, which is less than 7% of the typical average energy relative to MIX-Node-S). Notably, when the atomic positions of all atoms in the cluster models were allowed to relax, the agreement between the cluster and periodic calculations for the relative energies of the different isomers was degraded. This highlights the importance of including constraints imposed by the periodicity of the system when analyzing cluster models representing the nodes of MOFs.

Regardless of the chosen computational method or constraints, the MIX-Node-S topology, $[Zr_6(\mu_3-O)_4(\mu_3-OH)_4(OH)_4(H_2O)_4]^{8+}$, is predicted to be the thermodynamically most stable structure. For example, in the gas phase (i.e., activated), MIX-Node-S is 299 kJ mol^{-1} more stable in free energy than the OH-node and 236 kJ mol^{-1} more stable than the H_2O-node. This structure is also predicted to have the highest density of all computed structures, and its predicted unit cell volume of 22 960 Å^3 compares well with the experimental value of 23 005 Å^3.

An intriguing feature of the MIX-Node-S conformer is its hydrogen-bonding (H-bonding) motifs, for example the O1−H2···O2 motif shown in Figure 3. To assess the degree to which the O1−H2···O2 hydrogen bonding confers stability on MIX-Node-S, the hydrogen bonds were broken through
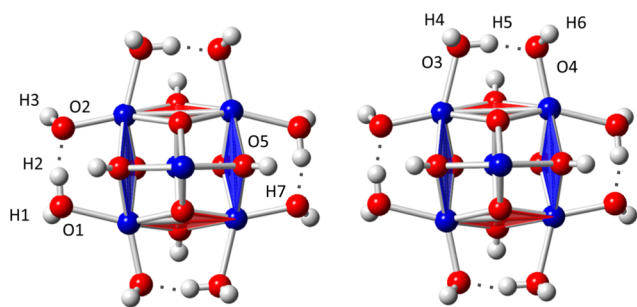
Figure 3. Atomic labels for several key stretching frequencies of the MIX-Node-S topology of NU-1000. The blue tetragonal faces point into the large mesoporous channels of NU-1000 (Figure 1c), while the red tetragonal faces point into the channels between the Kagome lattices (Figure 1d).

rotation of the aqua ligands about the Zr−O bond. The optimized structure with one such hydrogen bond broken is predicted to be 44 kJ/mol higher in electronic energy than the MIX-Node-S geometry; this difference can be taken as an upper bound for the relevant H-bond strength. Breaking all four H-bonds in this fashion raises the energy by 167 kJ/mol, which is still smaller than the energy difference between the MIX-Node-S and H_2O-Node topologies (i.e., 274 kJ/mol, Table 1). Hence, the MIX-Node-S topology with all four H2···O2 H-bonds broken is still more stable than the H_2O-Node by about 107 kJ/mol. This quantifies the importance of H-bonding in stabilizing the MIX-Node-S cluster, which we suspect may affect the reactivity, conductivity, and catalytic activity of NU-1000 and potentially other Zr_6-based MOFs. To our knowledge, this is the first mixed −OH and −OH$_2$ ligand motif proposed in the literature for a symmetrical Zr_6-based node. It is notable that mixed proton topologies have been proposed for asymmetric Zr_6-based nodes,[12] although no direct evidence for such a composition has been provided to date.

Considering additional factors that contribute to the stability of the MIX-Node-S topology, we examined oxygen partial charges computed from Charge Model 5[44] (CM5, chosen for its accuracy in reproducing electrical multipole moments, its ready applicability to all atoms in the periodic table, and its insensitivity to basis set). Interestingly, in the MIX-Node-S isomer, the charges on the O atoms are extremely uniform, being on average −0.667 au with a standard deviation of 0.052 au. By contrast, the O atoms in adjacent μ-oxo bridges in the cores of other MIX isomers have CM5 charges near 0 au (Table S3). The staggered (S) arrangement of protons on the core thus appears to permit optimal polarization of the Zr−O bonds consistent with the different electronegativities of the two atoms. Yang et al. have undertaken similar analyses of bonding and charge densities to rationalize the structures and stability of the Zr_6 MOFs UiO-66, -67, -68, and analogues.[45]

Finally, while gas-phase results are of interest for understanding the properties of the activated MOF, and for comparison to the "dry" IR spectra described below, it is also informative to consider the effects of aqueous solvation, as estimated from SMD continuum solvent calculations. As the higher energy isomers are less stable owing to electrostatic interactions less favorable than those found in the MIX-Node-S topology, it is unsurprising that solvation levels the energetic landscape (Table 1, ΔE values in parentheses in column 3). Nevertheless, the MIX-Node-S topology remains more than 100 kJ/mol more stable than any other.

Computational and Experimental IR Spectra. One attractive method to interrogate the proton topologies of NU-1000 is via IR spectroscopy. Given the agreement between the periodic calculations and the cluster approximations, as well as the significant reduction in computational cost, the vibrational frequencies for the OH-Node, H_2O-Node, and MIX-Node-S proton topologies were calculated utilizing the cluster models in order to compare against experiment. Again, the positions of the atoms in the aromatic rings were kept fixed during geometry optimizations, and therefore their vibrations (arising from the TBAPy^{4-} linker) are not observed in the theoretical IR spectra. The experimental IR spectrum—collected as diffuse reflectance spectra—for NU-1000 is shown in Figure 4
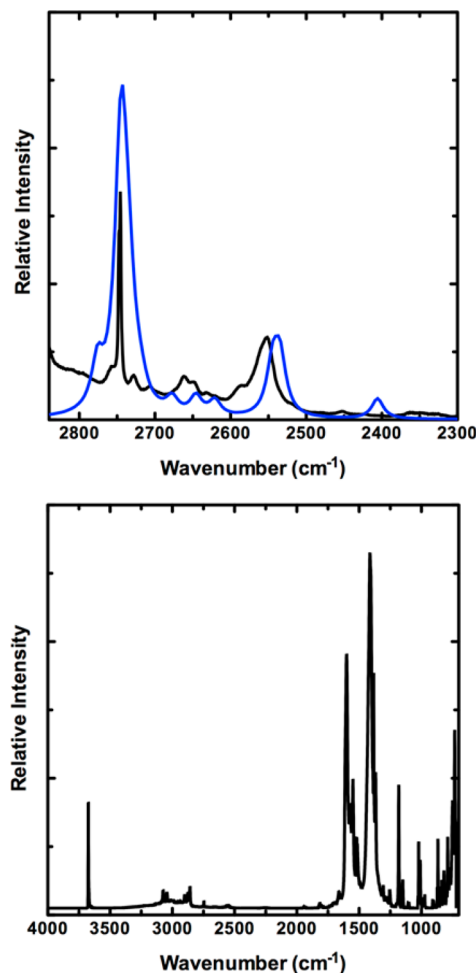

Figure 4. Full experimental DRIFTS spectra of NU-1000 (below) and highlights (above) of the H-bonded H_2O and −OH regions from 2300−2850 cm^{-1} for experiment (black) and theory summed over 4 isomers (blue; see text for details).

(bottom). A noteworthy feature of the experimental spectrum is a series of absorptions that are found below the C−H stretching region between 2400 and 2850 cm^{-1} as illustrated in Figure 4 (top).

Considering now results from the theoretical calculations, the key vibrational signatures for the −OH and −OH$_2$ ligands of the theoretical OH-Node and H_2O-Node topologies are cataloged in Table 2 together with several of the key experimental data. In the theoretical spectra for these two nodes, a number of peaks between 3600 and 3800 cm^{-1} are

Table 2. Key Vibrational Modes for the Theoretical OH-Node, H$_2$O-Node, and MIX-Node-S Topologies along with the Observed Experimental Vibrational Modes for NU-1000 and Their Corresponding Assignments[a]

	Wavenumber (cm^{-1})			
vibrational description	OH-Node theory	H$_2$O-Node theory	MIX-Node-S theory[b]	experimental[c]
non-H-bonded −OH stretch	3691	not present	3661−3664 3658−3663 3660, 3662 3662−3675	3674 (2957[d])
bridging μ_3-OH stretch	3609	not present	3652, 3655 3652−3655 3653, 3655 3652−3667	3674 (2957[d])
non-H-bonded H$_2$O stretch	not present	3584, 3588	3604−3608 3610, 3611, 3626 3616−3625 3604−3607, 3620	3672 (2957[d])
H-bonded H$_2$O/OH stretch	3472, 3469	not present	2727, 2743, 2746, 2754 2406, 2621, 2646, 2676 2515, 2533, 2544, 2551 2727, 2743, 2752, 2784	2745, 2747 (2214) 2625−2660 (2117−2144) 2551 (2061) 2745, 2747 (2214)

[a]In some instances the vibrational modes of the four faces of the Zr$_6$ node are decoupled in two sets; those involving the vibration of the OH/OH$_2$ ligands pointing inside the large pore within NU-1000 and those corresponding to the analogous mode pointing toward the smaller cavities. In addition, asymmetry in the overall structure may lead to additional peaks. Theoretical data are scaled by a factor of 0.939. [b]Results for 4 different MIX-Node-S topologies, differing as aquo/hydroxo positional or rotational isomers on the MIX-Node-S core, all predicted to be within 10 kJ/mol of one another in free energy (see Supporting Information for details). [c]Key peaks that shift on deuterium exchange are reported; deuterated frequencies are in parentheses. [d]This peak is difficult to assign precisely as it falls in the C−H stretching region.

predicted corresponding to the bridging and terminal −OH and −OH$_2$ stretching frequencies for each topology. Any or all of these might reasonably be assigned to correspond to the experimental peaks observed from 3672−3674 cm^{-1}. Importantly, however, *no* peaks in the region 2400−2900 cm^{-1} are predicted for either the OH-node or H$_2$O-node topologies.

For the global minimum MIX-Node-S topology shown in Figure 3, by contrast (top line in each row of 4 in the MIX-Node-S column of Table 2), in addition to high frequency peaks corresponding well with experiment, there are absorptions predicted from 2727 to 2754 cm^{-1}, corresponding to O−H stretches in hydrogen-bonded bridges between aquo and hydroxo ligands, that are in quite reasonable quantitative agreement with the experimental absorptions at 2745 and 2747 cm^{-1}. No peak, however, is predicted at lower frequency that might correspond to the experimentally observed absorption at 2551 cm^{-1}.

This observation led us to consider the possibility that other low energy MIX-Node-S isomers, i.e., MIX-Node-S topologies having alternative arrangements of aquo and hydroxo ligands, might be present at equilibrium such that the experimental spectrum may be a composite of their various individual spectra. By considering proton transfers from aquo to hydroxo ligands, and rotations of aquo ligands to reorient the *non*-hydrogen bonding proton of the −OH$_2$ unit, we identified 3 other isomers, ranging in energy from 8.4 to 10.0 kJ/mol above the global minimum (details in section S5 of the Supporting Information), and their predicted IR spectra are included in the additional rows in the MIX-Node-S column in Table 2. One of them (the third row) does indeed have absorptions predicted in the range from 2552−2589 cm^{-1}. As we do not expect our DFT calculations to be accurate enough to predict the Boltzmann population of isomers to better than about ±10 kJ/mol accuracy, we have used a direct comparison to the experimental spectrum to estimate the proportions, and Figure

4b includes a simulated spectrum assembled as 41% of the global minimum, and 9%, 16%, and 34% of the minor isomers in rows 2, 3, and 4 of the MIX-Node-S column in Table 2, respectively. As can be observed, the agreement between theory and experiment is overall quite reasonable.

Thus, qualitative comparison of the experimental DRIFTS spectrum to the theoretical IR spectra effectively rules out the OH-Node and H$_2$O-Node topologies. The most striking feature in the experimental spectrum is the combination of (inferred) concerted asymmetric stretches observed at 2551, 2747, and 2745 cm^{-1}, i.e., the stretches predicted for the isomers belonging to the MIX-Node-S topology.

Given the results of our computational effort, and additional IR spectroscopic studies detailed below, we have assigned the experimental peak centered around 3674 cm^{-1} to both the terminal and μ_3 bridging −OH groups. There is also a shoulder present at 3672 cm^{-1} (see the Supporting Information for further details), which has been assigned as the terminal H$_2$O stretching mode. We do also predict terminal and hydrogen-bonded H$_2$O bending modes at about 1550 and 1060 cm^{-1}, but these peaks fall in regions of the experimental spectrum dominated by absorptions from the organic ligands, so comparisons are not possible. The experimental spectra are also significantly broadened, and this may reflect the influence of trace amounts of solvent molecules of a second-sphere of solvation, the presence of which would be expected to influence the positions and shapes of the stretching frequencies or potentially some small amount of disorder that we observe, for example, in the single crystal X-ray structure of NU-1000. Irrespective of the absolute values of the frequencies, it is clear that only the MIX-Node-S topology is in acceptable agreement with our computational and experimental data.

D$_2$O Exchange Experiments and Variable Temperature DRIFTS. To further corroborate our proposed IR assignments, we turned to D$_2$O exchange and variable temperature DRIFTS

experiments. NU-1000 was submerged in D_2O and exchanged three times over the course of 72 h. After 72 h, the peak at 3674 cm^{-1} was significantly decreased, while the shoulder at 3672 cm^{-1} was no longer present (Figure 5a). The peaks at 2551,
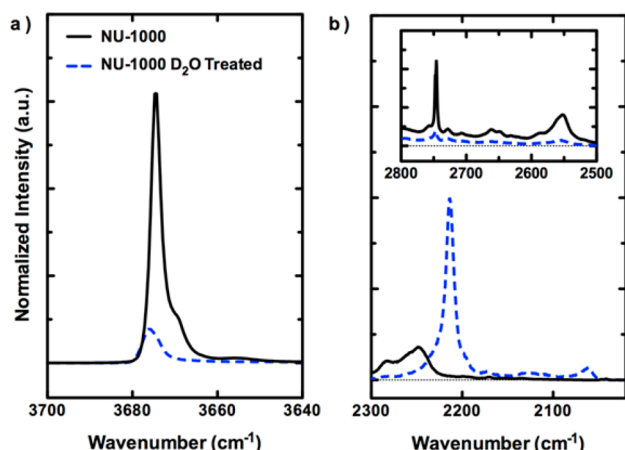

Figure 5. (a,b) The terminal and bridging −OH and −H_2O stretching regions of NU-1000 before (solid black line) and after exposure to D_2O (dotted blue line). The inset in panel b shows the H-bonded H_2O stretching features before and after exposure to D_2O.

2745, and 2747 cm^{-1} also disappear almost completely. At the same time, a new peak and shoulder appear at 2216 and 2213 cm^{-1}, and another new peak at 2061 cm^{-1} (Figure 5b). Interestingly, a portion of the peak at 3674 cm^{-1} remains in the deuterated spectrum. The results are consistent with both the terminal −OH and hydrogen bonding H_2O ligands being deuterated, but a possibly much slower exchange to deuterate the bridging μ_3-OH ligands, which may be sterically inaccessible.

The isotopic frequency ratios for the pairs of peaks 2747/2216, 2745/2213, and 2551/2061 are all about 1.24. Such a reduction from the harmonic oscillator value of about 1.4 is entirely consistent with the significant anharmonicity associated with strong hydrogen bonding. With respect to the OH stretch(es) at 3674 cm^{-1}, a similar scaling factor would place the corresponding OD stretch(es) at 2963 cm^{-1}. While this is in the C−H stretching region of the spectrum, and thus hard to assign definitively, nevertheless there does appear to be a new peak in the deuterated spectrum at 2957 cm^{-1} (Supporting Information). It is somewhat surprising that a frequency ratio closer to 1.4 is not observed for this isotope shift, but as no new peaks are observed below the C−H stretching region, we must conclude that the relevant O−D stretches are found there.

Next we turned to variable temperature DRIFTS measurements; the hydroxyl and H-bonded H_2O regions are highlighted in Figure 6. The symmetric (2747 cm^{-1}) and antisymmetric (2745 cm^{-1}) H-bonded H_2O stretches disappear between 150 and 250 °C presumably via ligand dissociation. Concomitant to the loss of the H-bonded H_2O molecules, the hydroxyl region starts to disappear at 150 °C, and completely disappears by 300 °C. It is well-known that the bridging −OH ligands in UiO-66 (another Zr_6-based MOF node) condense and release water around 300 °C, and we suspect that a similar phenomenon is observed here.[46,47] It is noteworthy that complete dehydration of the NU-1000 node would correspond to a mass loss of 6.6% and we observe such a mass loss over a similar temperature range (see Supporting Information). At
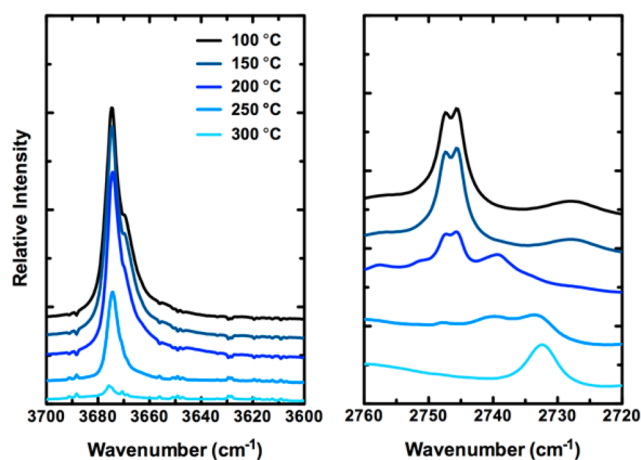

Figure 6. Temperature-dependent DRIFTS spectra of the −OH and H-bonded H_2O regions for NU-1000.

high temperature, a peak at 2732 cm^{-1} is observed. While the number of possible dehydrated structures makes it difficult to assess anything computationally, it may be that some dehydration occurs with loss of oxygen atoms in the core, as has been observed for UiO-66,[47] and core rearrangement leads to a local hydrogen bond that persists until still higher temperatures are reached. In any case, the D_2O- and temperature-dependence of the stretches at 2745 and 2747 cm^{-1} excludes the possibility that these are unusually low C−H stretches from the TBAPy^{4-} linker of NU-1000.

Computational Efforts to Address the Loss of the H-Bonded H_2O Molecules and Condensation of −OH Ligands. It is of interest to address and understand the origin of the observed disappearance of the −OH and −OH_2 peaks in the IR spectra. Hence we investigated the energetic costs associated with removing the H-bonded H_2O ligands and the condensation of −OH groups to form H_2O. Calculations indicate that the energetic cost to remove one aqua ligand is 145 kJ/mol, while the energy required to remove all four coordinated water molecules is 565 kJ/mol. (These are constrained electronic energies optimized with the aromatic rings frozen.) This ratio of approximately 4 suggests that there is no special cooperativity associated with addition or removal of individual aqua ligands. Thus, conversion of the MIX-Node-S to the H_2O-Node with subsequent H_2O ligand dissociation can take place upon heating (vide supra). The energy to transfer one proton (H7) from a bridging OH-group to a terminal one is 89 kJ/mol. As such, we speculate that the loss of the −OH and −OH_2 stretches in the IR spectra occurs via thermal proton transfer followed by elimination of −OH_2 ligands. These benchmarking energies should prove useful for rationalizing the stability and predicting the nodal reactivity of Zr_6-based MOFs.

By employing a combined quantum chemical and experimental approach we have been able to assign a staggered mixed proton topology, $[Zr_6(\mu_3\text{-}O)_4(\mu_3\text{-}OH)_4(OH)_4(H_2O)_4]^{8+}$, to the Zr_6-based MOF NU-1000 while simultaneously ruling out five alternative proton topologies. Within the mixed proton topology, multiple isomers appear to be present at room temperature differing in arrangements of coordinating aquo and hydroxo ligands. This is the first time a mixed node proton topology has been determined for a MOF. We anticipate that this unique H-bonded motif will have wide ranging implications in applications including acid/base chemistry, conductivity, catalysis, and in understanding NU-1000s reactivity toward

functionalization (e.g., AIM and SALI). Results from ongoing work in our laboratories consistent with these assessments will be reported in due course.

■ ASSOCIATED CONTENT

Ⓢ Supporting Information

Additional computational details, DRIFTS, PXRD, and TGA data can be found in the Supporting Information. This material is available free of charge via the Internet at http://pubs.acs.org.

■ AUTHOR INFORMATION

Corresponding Authors
*E-mail: cramer@umn.edu (C.J.C.).
*E-mail: j-hupp@northwestern.edu (J.T.H.).
*E-mail: o-farha@northwestern.edu (O.K.F.).
*E-mail: gagliard@umn.edu (L.G.).

Author Contributions
‖N.P. and J.E.M. contributed equally to this work.

Notes
The authors declare no competing financial interest.

■ ACKNOWLEDGMENTS

■ REFERENCES

(1) Férey, G. Hybrid Porous Solids: Past, Present, Future. *Chem. Soc. Rev.* **2007**, *37*, 191−214.

(2) Horike, S.; Shimomura, S.; Kitagawa, S. Soft Porous Crystals. *Nat. Chem.* **2009**, *1*, 695−704.

(3) Furukawa, H.; Cordova, K. E.; O'Keefe, M. O.; Yaghi, O. M. The Chemistry and Applications of Metal−Organic Frameworks. *Science* **2013**, *341*, 1230444.

(4) Roy, S.; George, C. B.; Ratner, M. A. Catalysis by a Zinc-Porphyrin-Based Metal−Organic Framework: From Theory to Computational Design. *J. Phys. Chem. C* **2012**, *116*, 23494−23502.

(5) Planas, N.; Dzubak, A. L.; Poloni, R.; Lin, L.-C.; McManus, A.; McDonald, T. M.; Neaton, J. B.; Long, J. R.; Smit, B.; Gagliardi, L. The Mechanism of Carbon Dioxide Adsorption in an Alkylamine-Functionalized Metal−Organic Framework. *J. Am. Chem. Soc.* **2013**, *135*, 7402−7405.

(6) Oxford, G. A. E.; Dubbeldam, D.; Broadbelt, L. J.; Snurr, R. Q. Elucidating Steric Effects on Enantioselective Epoxidation Catalyzed by (Salen)Mn in Metal−Organic Frameworks. *J. Mol. Catal. A: Chem.* **2011**, *334*, 89−97.

(7) Farha, O. K.; Yazaydın, A. Ö.; Eryazici, I.; Malliakas, C. D.; Hauser, B. G.; Kanatzidis, M. G.; Nguyen, S. T.; Snurr, R. Q.; Hupp, J. T. De Novo Synthesis of a Metal−Organic Framework Material Featuring Ultrahigh Surface Area and Gas Storage Capacities. *Nat. Chem.* **2010**, 944−948.

(8) Wilmer, C. E.; Leaf, M.; Lee, C. Y.; Farha, O. K.; Hauser, B. G.; Hupp, J. T.; Snurr, R. Q. Large-Scale Screening of Hypothetical Metal−Organic Frameworks. *Nat. Chem.* **2012**, *4*, 83−89.

(9) Cavka, J. H.; Jakobsen, S.; Olsbye, U.; Guillou, N.; Lamberti, C.; Bordiga, S.; Lillerud, K. P. A New Zirconium Building Brick Forming Metal Organic Frameworks with Exceptional Stability. *J. Am. Chem. Soc.* **2008**, *130*, 13850−13851.

(10) Morris, W.; Volosskiy, B.; Demir, S.; Gándara, F.; McGrier, P. L.; Furukawa, H.; Cascio, D.; Stoddart, F. J.; Yaghi, O. M. Synthesis, Structure and Metalation of Two New Highly Porous Zirconium Metal−Organic Frameworks. *Inorg. Chem.* **2012**, 6443−6445.

(11) Furukawa, H.; Gándara, F.; Zhang, Y.-B.; Jiang, J.; Queen, W. L.; Hudson, M. R.; Yaghi, O. M. Water Adsorption in Porous Metal−Organic Frameworks and Related Materials. *J. Am. Chem. Soc.* **2014**, *136*, 4369−4381.

(12) Jiang, H.-L.; Feng, D.; Wang, K.; Gu, Z.-Y.; Wei, Z.; Chen, Y.-P.; Zhou, H.-C. J. An Exceptionally Stable, Porphyrinic Zr Metal−Organic Framework Exhibiting pH-Dependent Fluorescence. *J. Am. Chem. Soc.* **2013**, *135*, 13934−13938.

(13) Wu, H.; Chua, Y. S.; Krungleviciute, V.; Tyagi, M.; Chen, P.; Yildirim, T.; Zhou, W. Unusual and Highly Tunable Missing-Linker Defects in Zirconium Metal−Organic Framework UiO-66 and Their Important Effects on Gas Adsorption. *J. Am. Chem. Soc.* **2013**, *135*, 10525−10532.

(14) Chavan, S.; Vitillo, J. G.; Gianolio, D.; Zavorotynska, O.; Civalleri, B.; Jakobsen, S.; Nilsen, M. H.; Valenzano, L.; Lamberti, C.; Lillerud, K. P.; Bordiga, S. H_2 Storage in Isostructural UiO-67 and UiO-66 MOFs. *Phys. Chem. Chem. Phys.* **2012**, *14*, 1614−1626.

(15) Yang, Q.; Guillerm, V.; Ragon, F.; Wiersum, A. D.; Llewellyn, P. L.; Zhong, C.; Devic, T.; Serre, C.; Maurin, G. CH_4 Sotrage and CO_2 Capture in Highly Porous Zirconium Oxide Base Metal−Organic Frameworks. *Chem. Commun.* **2012**, *48*, 9831−9833.

(16) Vermoortele, F.; Vandichel, M.; Van de Voorde, B.; Ameloot, R.; Waroquier, M.; Van Speybroeck, V.; De Vos, D. E. Electronic Effects of Linker Substitution on Lewis Acid Catalysis with Metal−Organic Frameworks. *Angew. Chem., Int. Ed.* **2012**, *51*, 4887−4890.

(17) Siu, P. W.; Brown, Z. J.; Farha, O. K.; Hupp, J. T.; Scheidt, K. A. A Mixed Dicarboxylate Strut Approach to Enhancing Catalytic Activity of a *De Novo* Urea Derivative of Metal−Organic Framework UiO-67. *Chem. Commun.* **2013**, *49*, 10920−10922.

(18) Vermoortele, F.; Bueken, B.; Le Bars, G.; Van de Voorde, B.; Vandichel, M.; Houthoofd, K.; Vimont, A.; Daturi, M.; Waroquier, M.; Van Speybroeck, V.; Kirschhock, C.; De Vos, D. E. Synthesis Modulation as a Tool To Increase the Catalytic Activity of Metal−Organic Frameworks: The Unique Case of UiO-66(Zr). *J. Am. Chem. Soc.* **2013**, *135*, 11465−11468.

(19) Katz, M. J.; Mondloch, J. E.; Totten, R. K.; Park, J. K.; Nguyen, S. T.; Farha, O. K.; Hupp, J. T. Simple and Compelling Biomimetic Metal−Organic Framework Catalyst for the Degradation of Nerve Agent Simulants. *Angew. Chem., Int. Ed.* **2013**, *53*, 497−501.

(20) Carboni, M.; Abney, C. W.; Liu, S.; Lin, W. Highly Porous and Stable Metal−Organic Frameworks for Uranium Extraction. *Chem. Sci.* **2013**, *4*, 2396−2402.

(21) Yee, K.-K.; Reimer, N.; Liu, J.; Cheng, S.-Y.; Yiu, S.-M.; Weber, J.; Stock, N.; Xu, Z. Effective Mercury Sorption by Thiol-Laced Metal−Organic Frameworks: In Strong Acid and the Vapor Phase. *J. Am. Chem. Soc.* **2013**, *135*, 7795−7798.

(22) Ameloot, R.; Aubrey, M.; Wiers, B. M.; Gómora-Figueroa, A. P.; Patel, S. N.; Balsara, N. P.; Long, J. R. Ionic Conductivity in the Metal−Organic Framework UiO-66 by Dehydration and Insertion of Lithium *tert*-Butoxide. *Chem.—Eur. J.* **2013**, *19*, 5533−5536.

(23) Nickerl, G.; Leistner, M.; Helten, S.; Bon, V.; Senkovska, I.; Kaskel, S. Integration of Accessible Secondary Metal Sites into MOFs for H_2S Removal. *Inorg. Chem. Front.* **2014**, *1*, 325−330.

(24) Feng, D.; Gu, Z.-Y.; Li, J.-R.; Jiang, H.-L.; Wei, Z.; Zhou, H.-C. Zirconium-Metalloporphyrin PCN-222: Mesoporous Metal−Organic Frameworks with Ultrahigh Stability as Biomimetic Catalysts. *Angew. Chem., Int. Ed.* **2012**, *51*, 10307−10310.

(25) Chen, Y.; Hoang, T.; Ma, S. Biomimetic Catalysis of a Porous Iron-Based Metal−Metalloporphyrin Framework. *Inorg. Chem.* **2012**, *51*, 12600−12602.

(26) Mondloch, J. E.; Bury, W.; Fairen-Jimenez, D.; Kwon, S.; DeMarco, E. J.; Weston, M. H.; Sarjeant, A. A.; Nguyen, S. T.; Stair, P. C.; Snurr, R. Q.; Farha, O. K.; Hupp, J. T. Vapor-Phase Metallation by Atomic Layer Deposition In a Metal−Organic Framework. *J. Am. Chem. Soc.* **2013**, *135*, 10294−10297.

(27) Deria, P.; Mondloch, J. E.; Tylianakis, E.; Ghosh, P.; Bury, W.; Snurr, R. Q.; Hupp, J. T.; Farha, O. K. Perfluoroalkane Functionalization of NU-1000 via Solvent-Assisted Ligand Incorporation: Synthesis and CO_2 Adsorption Studies. *J. Am. Chem. Soc.* **2013**, *135*, 16801−16804.

(28) Deria, P.; Bury, W.; Hupp, J. T.; Farha, O. K. Versatile Functionalization of the NU-1000 Platform by Solvent-Assisted Ligand Incorporation. *Chem. Commun.* **2014**, *50*, 1965−1968.

(29) It is worth noting that compared to the "fully saturated" $Zr_6(O)_8(H)_4(RCO_2)_{12}$ containing nodes such as the UiO series, the $Zr_6(O)_8(O)_8(H)_{16}(RCO_2)_8$ containing nodes in NU-1000 exhibit a significant degree of complexity with respect to their proton topology.

(30) Kresse, G.; Furthmüller, J. Efficient Iterative Schemes for *Ab Initio* Total-Energy Calculations Using a Plane-Wave Basis Set. *Phys. Rev. B* **1996**, *54*, 11169−11186.

(31) Kresse, G.; Hafner, J. *Ab Initio* Molecular-Dynamics Simulation of the Liquid−Metal−Amorphous-Semiconductor Transition in Germanium. *Phys. Rev. B* **1994**, *49*, 14251−14269.

(32) Kresse, G.; Hafner, J. Ab Initio Molecular Dynamics for Liquid Metals. *Phys. Rev. B* **1993**, *47*, 558−561.

(33) Kresse, G.; Furthmüller, J. Efficiency of Ab-Initio Total Energy Calculations for Metals and Semiconductors Using a Plane-Wave Basis Set. *Comput. Mater. Sci.* **1996**, *6*, 15−50.

(34) Perdew, J. P.; Wang, Y. Accurate and Simple Analytic Representation of the Electron-Gas Correlation Energy. *Phys. Rev. B* **1992**, *45*, 13244−13249.

(35) Perdew, J. P.; Burke, K.; Ernzerhof, M. Generalized Gradient Approximation Made Simple. *Phys. Rev. Lett.* **1996**, *77*, 3865−3868.

(36) Perdew, J. P.; Emzerhof, M.; Burke, K. Rationale for Mixing Exact Exchange with Density Functional Approximations. *J. Chem. Phys.* **1996**, *105*, 9982−9985.

(37) Zhao, Y.; Truhlar, D. G. A New Local Density Functional for Main-Group Thermochemistry, Transition Metal Bonding, Thermochemical Kinetics, and Noncovalent Interactions. *J. Chem. Phys.* **2006**, *125*, 194101.

(38) Frisch, M. J.; Trucks, G. W.; Schlegel, H. B.; Scuseria, G. E.; Robb, M. A.; Cheeseman, J. R.; Scalmani, G.; Barone, V.; Mennucci, B.; Petersson, G. A. et al. *Gaussian 09*, revisions B.01 and A.02; Gaussian, Inc.: Wallingford, CT, 2009.

(39) Zhao, Y.; Peverari, R.; Yang, K.; Truhlar, D. G. *MN-GFM*, version 6.4; University of Minnesota: Minneapolis, MN, 2012.

(40) Hehre, W. J.; Radom, L.; Schleyer, P. v. R.; Pople, J. A. *Ab Initio Molecular Orbital Theory*; Wiley: New York, 1986.

(41) Martin, J. M. L.; Sundermann, A. Correlation Consistent Valence Basis Sets for Use with the Stuttgart−Dresden−Bonn Relativistic Effective Core Potentials: The Atoms Ga−Kr and In−Xe. *J. Chem. Phys.* **2001**, *114*, 3408−3420.

(42) Marenich, A. V.; Cramer, C. J.; Truhlar, D. G. Universal Solvation Model Based on Solute Electron Density and on a Continuum Model of the Solvent Defined by the Bulk Dielectric Constant and Atomic Surface Tensions. *J. Phys. Chem. B* **2009**, *113*, 6378−6396.

(43) We previously reported the DRIFTS of NU-1000 and tentatively assigned the observed vibrational stretches at 3674 cm^{-1} and 3655 cm^{-1} as terminal and μ_3 bridging −OH stretches. This assignment would be consistent with the NU-1000-OH topology. Re-examination of our DRFTS data in light of the computational and experimental efforts described herein, revealed that the stretch at 3655 cm^{-1} is highly susceptible to trace amounts of weakly bound solvent molecules (likely H_2O, but potentially DMF or acetone molecules that are present as a result of the synthesis NU-1000) that can be removed from the system at 120 °C. A comparison of a NU-1000 DRIFTS spectra taken immediately after activation at 120 °C under dynamic vacuum, to one taken after sitting under ambient atmospheric conditions is shown in the Supporting Information. Clearly the stretch at 3655 cm^{-1} was removed under these activation conditions.

(44) Marenich, A. V.; Jerome, S. V.; Cramer, C. J.; Truhlar, D. G. Charge Model 5: An Extension of Hirshfeld Population Analysis for the Accurate Description of Molecular Interactions in Gaseous and Condensed Phases. *J. Chem. Theory Comput.* **2012**, *8*, 527−541.

(45) Yang, L.-M.; Ganz, E.; Svelle, S.; Tilset, M. Computational Exploration of Newly Synthesized Zirconium Metal−Organic Frameworks UiO-66, -67, -68 and Analogues. *J. Mater. Chem. C* **2014**, *2*, 7111−7125.

(46) Valenzano, L.; Civalleri, B.; Chavan, S.; Bordiga, S.; Nilsen, M. H.; Jakobsen, S.; Lillerud, K. P.; Lamberti, C. Disclosing the Complex Structure of UiO-66 Metal Organic Framework: A Synergic Combination of Experiment and Theory. *Chem. Mater.* **2011**, *23*, 1700−1718.

(47) Shearer, G.; Forselv, S.; Chavan, S.; Bordiga, S.; Mathisen, K.; Bjørgen, M.; Svelle, S.; Lillerud, K. In Situ Infrared Spectroscopic and Gravimetric Characterisation of the Solvent Removal and Dehydroxylation of the Metal Organic Frameworks UiO-66 and UiO-67. *Topics Catal.* **2013**, *56*, 770−782.

3723

dx.doi.org/10.1021/jz501899j | *J. Phys. Chem. Lett.* 2014, 5, 3716−3723